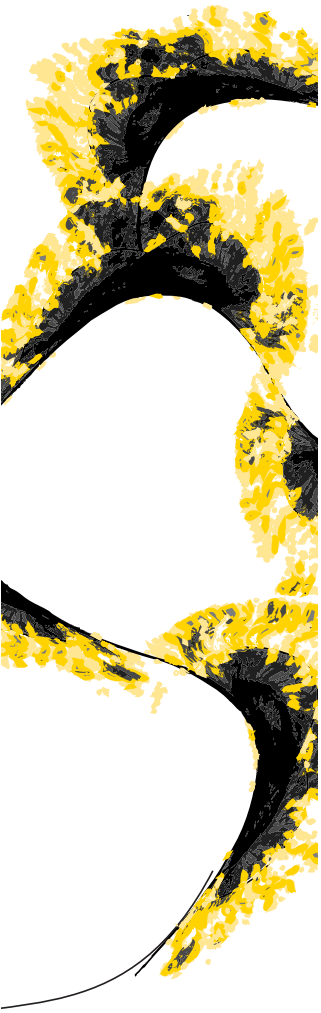

RAM ROBOTICS AND MECHATRONICS

REAL-TIME MRI-GUIDED NEEDLE TRACKING FOR INTERVENTIONAL PROCEDURES

Z.J. (Zhi-Jian) Tai

MSC ASSIGNMENT

Committee:
prof. dr. ir. S. Stramigioli
dr. ir. K. Niu
dr. ir. W.M. Brink
dr. V. Groenhuis, MSc
dr. J. Dasdemir

October, 2024

067RaM2024
Robotics and Mechatronics
EEMCS
University of Twente
P.O. Box 217
7500 AE Enschede
The Netherlands

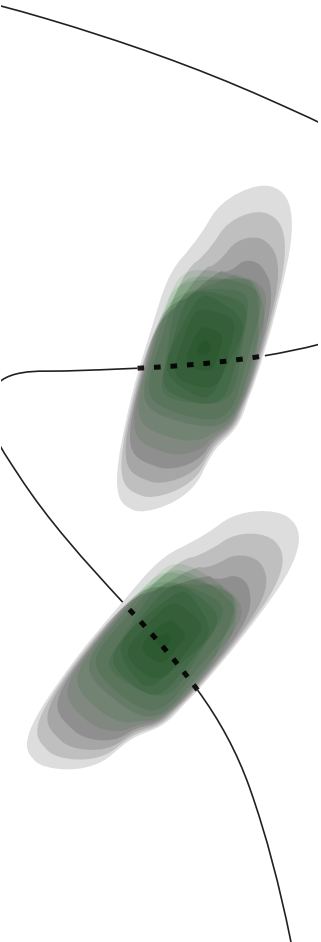

UNIVERSITY OF TWENTE. | TECHMED CENTRE UNIVERSITY OF TWENTE. | DIGITAL SOCIETY INSTITUTE

Real-time MRI-guided needle tracking for interventional procedures

Zhi Jian Tai[1], Vincent Groenhuis[1], Wyger Brink[2], Stefano Stramigioli[1], Idse Kuijper[1], Kenan Niu[1]

***Abstract*— Traditional MRI-guided breast biopsies are often time-consuming and prone to errors due to manual manipulation. To overcome these challenges, the Sunram7 robotic system was developed for autonomous biopsy. However, the robotic system suffers from inaccurate needle positioning due to pneumatic stepper motor skipping. To address this, we developed a real-time MRI 2D slice plane control strategy algorithm. This algorithm provides the robotic system with visual feedback of the needle trajectory and breast deformation in an MRI environment. By utilizing three real-time 2D MRI slices, we accurately determined the needle tip position and orientation. This feedback enables the robotic system to dynamically adjust the needle trajectory, resulting in improved hit rates of target lesions. Experiments conducted in a controlled MRI environment demonstrated the effectiveness of our approach. The needle track algorithm achieved an average tip localization accuracy of 1.179 $\pm$ 0.385 mm. Moreover, biopsy times were significantly reduced to 13.5 $\pm$ 2.5 minutes, compared to the traditional method with an average duration of 38 minutes. Overall, our method showcases the potential of real-time feedback to enhance the precision and efficiency of robotic systems in interventional procedures.**

I. Introduction

Yearly, there are over 2.3 million cases of breast cancer worldwide, with 95% of countries reporting it as the first or second leading cause of female cancer deaths [1]. Early detection and intervention are crucial in combating this disease, as evidenced by the 5-year relative survival rate of over 80% for breast cancer patients diagnosed early [2]. Various imaging techniques, such as mammography, ultrasound, and Magnetic Resonance Imaging (MRI), aid in breast cancer diagnosis. MRI has become an essential tool for guiding minimally invasive procedures, particularly in interventional radiology, due to its superior visualization of lesions in soft tissue compared to other imaging modalities [3]. Once a suspicious lesion is identified, a needle-based biopsy should be performed to determine if the lesion is benign or malignant, and treated accordingly.

However, current MRI-guided procedures are often more time-consuming than those using other imaging techniques. This is due to the multiple steps involved, including moving the patient in and out of the gantry to assess needle progression and manually inspecting multiple MRI slices to verify needle trajectory. To address these challenges, the MR-safe breast biopsy robotic system, Sunram7 was developed [4]. Figure 1 shows the operator field of view in the MRI control room. The robotic system is entirely produced from 3D plastic printed components, which makes it able to be used in an MR environment. However, the system has limitations. One notable issue is the potential for skipping steps in the pneumatic stepper motors, due to loss of pressure. This means the robot's joint angles don't perfectly match its assumed position, resulting in systematic errors at the end-effector that impact needle insertion. Implementing feedback control can help mitigate this misalignment. There are multiple options for giving feedback, as for this work the aim is to give a visual real-time feedback of the needle trajectory and the deformation of the breast. Therefore, the primary objective of this work is to track and give feedback back to the controller on the error offset of the assumed and the real needle position. Several challenges must be overcome to achieve this. For instance, oblique needle insertion can lead to the needle appearing in multiple adjacent MRI slices when viewed on coronal/sagittal-oriented slices. There needs to be a way to obtain a refined slice where the needle is seen fully in one 2D MRI scan. Additionally, susceptibility artifacts caused by metallic objects within the MRI disrupt the signal, obscuring the needle's geometry and presenting it as a loss of signal. Biopsy needles, typically made of titanium, manifest as dark pixels with noticeable artifacts surrounding and on them. The shape and intensity of these artifacts vary significantly depending on the needle's angle relative to the main magnetic field B_0 and needle property, affecting its visibility and differentiation from surrounding tissues [5]. Finally, real-time updates of all image planes are crucial to prevent losing track of the needle during the

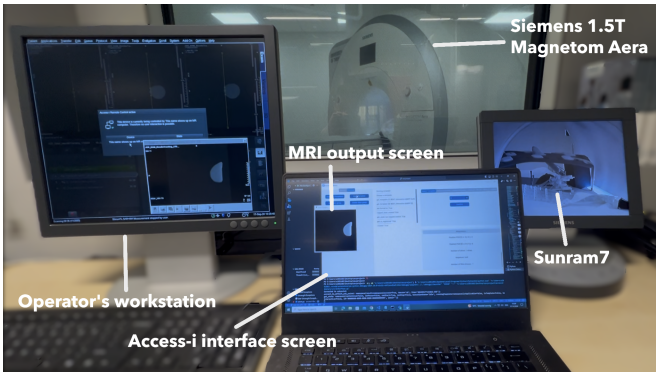

Fig. 1: The operator field of view, when using the Access-i interface. The Access-i interface provides real-time monitoring of the needle position and MRI slice projections.

[1] Robotics and Mechatronics, University of Twente, Enschede, 7500AE, The Netherlands z.j.tai@student.utwente.nl (Z.J.), k.niu@utwente.nl (K.N.), v.groenhuis@utwente.nl (V.G.), s.stramigioli@utwente.nl (S.S.), i.kuijper@student.utwente.nl (I.K)

[2]Magnetic Detection and Imaging group, TechMed Centre, University of Twente, Enschede, 7500AE, The Netherlands w.m.brink@utwente.nl (W.B.)

procedure. Based on the objectives, the following research question can be formulated as:

How can a 2D real-time MRI image plane update algorithm be designed to consider both the information derived from MRI images and the robotic kinematics to achieve optimal tracking performance?

This work aims to develop a real-time MRI-guided needle-tracking algorithm for interventional procedures. The main contributions of this paper are as follows:

1) Needle 3D localization: fast needle segmentation using deep learning, quantifying the position and orientation of the needle tip and entry point in MRI 3D volume.
2) Real-time MRI 2D slice plane control strategy: taking both needle position and orientation derived from MRI images and robotic kinematics into account to always obtain the biopsy needle in one MRI slice.

II. State-of-the-art

Supervised deep learning, using convolutional neural networks (CNNs), has demonstrated promising results in image classification and segmentation within the medical imaging domain [6][7][8]. Minimally invasive needle procedures offer significant advantages for patient care. However, ensuring accurate needle placement remains a critical challenge for clinicians, particularly in MRI due to susceptibility artifacts and the variability in needle appearance. Li et al. utilized a 2D Mask R-CNN model for needle detection and localization on intra-procedural and real-time MR images in the prostate [9]. The results demonstrated that the Mask R-CNN-based algorithm could track the needle tip and its orientation. Their method to estimate the needle axis (centerline) was to apply Orthogonal distance regression (ODR) to the needle segmentation mask. The point along the detected needle axis was used to identify the needle feature tip. However, there are some limitations to this approach. When the needle's axis is significantly obliqued to the image pane, there is a chance that the algorithm will miss the needle detection. Another limitation is that the output of the model is limited to 2D, which means that the coordinates of the segmented needle mask and detection are in the 2D coordinate of the MRI slice. Li et al. made improvements with a physics-based simulation using FORECAST of the needle artifacts for extending its training dataset to enhance the accuracy of the Mask-RCNN [10]. Subsequently, Zhou et al. employ a coarse-to-fine strategy, utilizing 3D Swin UNETR for initial needle feature segmentation and 2D Swin Transformer for refined segmentation and localization primarily on the liver as the organ of interest [11]. In contrast, Mehrtash et al. developed an asymmetric 3D FCN for needle detection, achieving good accuracy and fast prediction times, but considered a very large dataset of 583 MRI scans from 71 patients [12]. The performance of the system was found to be comparable to that of an expert human observer, demonstrating its potential for clinical use in improving the efficiency and accuracy of MRI-guided prostate biopsies. These developments show how deep learning can greatly improve needle localization in MRI, making image-guided procedures safer and more effective.

III. Methods and materials

In this work, we investigated the feasibility of real-time MRI dynamic needle tracking for interventional procedures, using only three real-time 2D MRI scans as input for the pipeline. During the experiments, MRI-guided targeted needle placement will be performed in the breast phantom using the robotic system Sunram7 [4]. The proposed pipeline for real-time needle tracking is illustrated in Figure 2. The following sections will detail the test setup, MRI dataset selection, segmentation model architecture, and system overview.

A. Test setup and experiential overview

The MRI-guided targeted needle placement is performed in a PVC Plastisol and gelatine-based breast phantom on a 1.5T MRI scanner (SIEMENS 1.5T MAGNETOM Aera, Siemens Healthineers, Erlangen, Germany). The scanner utilized two separate coils for signal reception: an 18-channel torso coil and a 24-channel spine coil. Figure 2 represents the workflow of the process. The Access-i interface is used to control the position and the orientation of the MRI slices. The screen also represents the real-time images coming from the MRI.

TABLE I: 3D dataset and 2D dataset

	3D dataset	2D dataset
FOV	288x288x192	288x288
Orientation	Axial	Oblique
Number of slices	128	1
In-plane resolution	1.5x1.5mm^2	1.5x1.5mm^2
In-plane matrix size	192x192	192x192
Slice thickness	1.5 mm	5 mm
Flip angle	40	40
Acquisition time	1min 32s	1s
Size of dataset	53	701

B. MRI Dataset of biopsy needle

3D T2-weighted TrueFISP and 2D balanced steady-state free precession (bSSFP) images were collected during the experiments. The obtained dataset, detailed in Table I, was used to define two classes for needle feature annotation. Class 1 focuses on the axial orientation. The needle, being a long thin cylinder, appears as a series of circular cross-sections in axial plane images when inserted into the breast phantom. The size and position of these circles vary depending on the needle's angle and trajectory. This characteristic shape allows for manual annotation of the circular cross-section in each slice of the 3D dataset. The second class aims to visualize the full needle in a single refined slice. To achieve this, the MRI slice needs to be aligned with the needle's trajectory, as this allows the entire needle to be captured within a single plane. Using the determined needle path and angle of insertion, an oblique slice can be obtained where

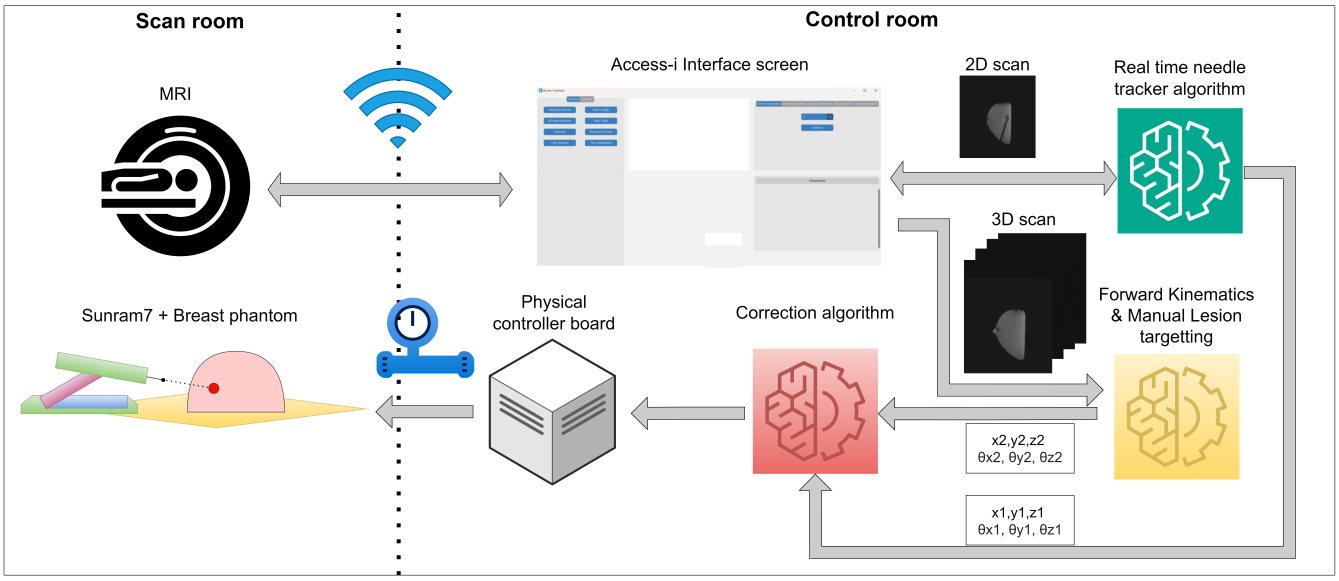

Fig. 2: The Schematic overview of all the components of the system. The Access-i interface establishes two-way communication with the MRI scanner and simultaneously communicates with the needle tracker algorithm to obtain the optimal real-time MRI slice of the needle. The calculation of the position and orientation of the needle from both the needle tracker and forward kinematics are relayed to the correction algorithm. From the correction, the offset between the assumed and real needle position is calculated. The offset is then passed on to the physical controller board, which transforms the pneumatics stepper motor of the Sunram7 into movement.

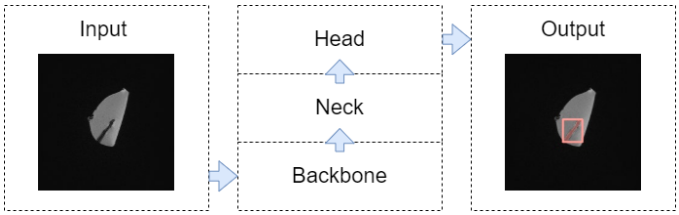

Fig. 3: Simplified overview of the YOLOv8-segmentation architecture. Consisting of the backbone, neck and head structure.

the needle appears as a long, thin, continuous line extending from its entry point to its tip within the breast phantom. However, potential image artifacts may obscure or distort the needle's appearance. Despite this, the characteristic linear shape in the oblique slice allows for manual annotation.

Both classes were annotated using Roboflow [13], a platform that provides tools to upload and manually annotate images.

C. Needle segmentation architecture

This work utilizes the YOLOv8 segmentation architecture (Fig. 3), pretrained on the COCO dataset. YOLOv8 is a state-of-the-art real-time object detection and instance segmentation model developed by Glenn Jocher and the Ultralytics team[14]. YOLOv8 provides different models with sizes and complexities: 'small', 'medium', 'large', and 'extra-large'. Before choosing YOLOv8, we compared other instance segmentation algorithms, such as Mask-RCNN [15], U-Net [16]. However, the YOLOv8 algorithm has been showing strong performance in object detection, and especially the real-time detection capability has been a great factor in choosing this algorithm.

Figure 3 represents the model. The model is an anchor-free detection model, which makes it a powerful tool for fast real-time computer vision tasks. The architecture can be divided into the backbone, neck and head parts, each consisting of different blocks. The **convolution block** is responsible for extracting the image features. Whereas the **C2f block** is responsible for splitting the incoming feature map into two branches, *bottleneck branch* and the *identity branch*. The bottleneck block is designed to extract the spatial feature, whereas the identity branch acts as a skip connection. The **SPPF** (Spatial Pyramid Pooling Fast) **block** is used after the C2f block. It consists of multiple max-pooling operations of different sizes. Which generates a collection of feature maps, where contextual information can be enhanced, this is utilized so the the model can extract features across multiple dimensions. The **upsample block** increases the feature map by double, without changing the output channel. The **concat block** sums of the without changing the resolutions. And at last, there are three **segment blocks**. Where the first and third block specialises in detecting small objects, whereas the second block specialises in medium-sized objects.

The loss function consists of a combined loss of bounding box loss (L_box), classification loss (L_cls), segmentation loss (L_seg) and distribution focal loss (L_dfl). The loss function is defined as the weighted sum of the three components: $L_{total} = \lambda_{box} * L\_box + \lambda_{cls} * L\_cls + \lambda_{dfl} * L\_dfl + \lambda_{seg} * L\_seg$.

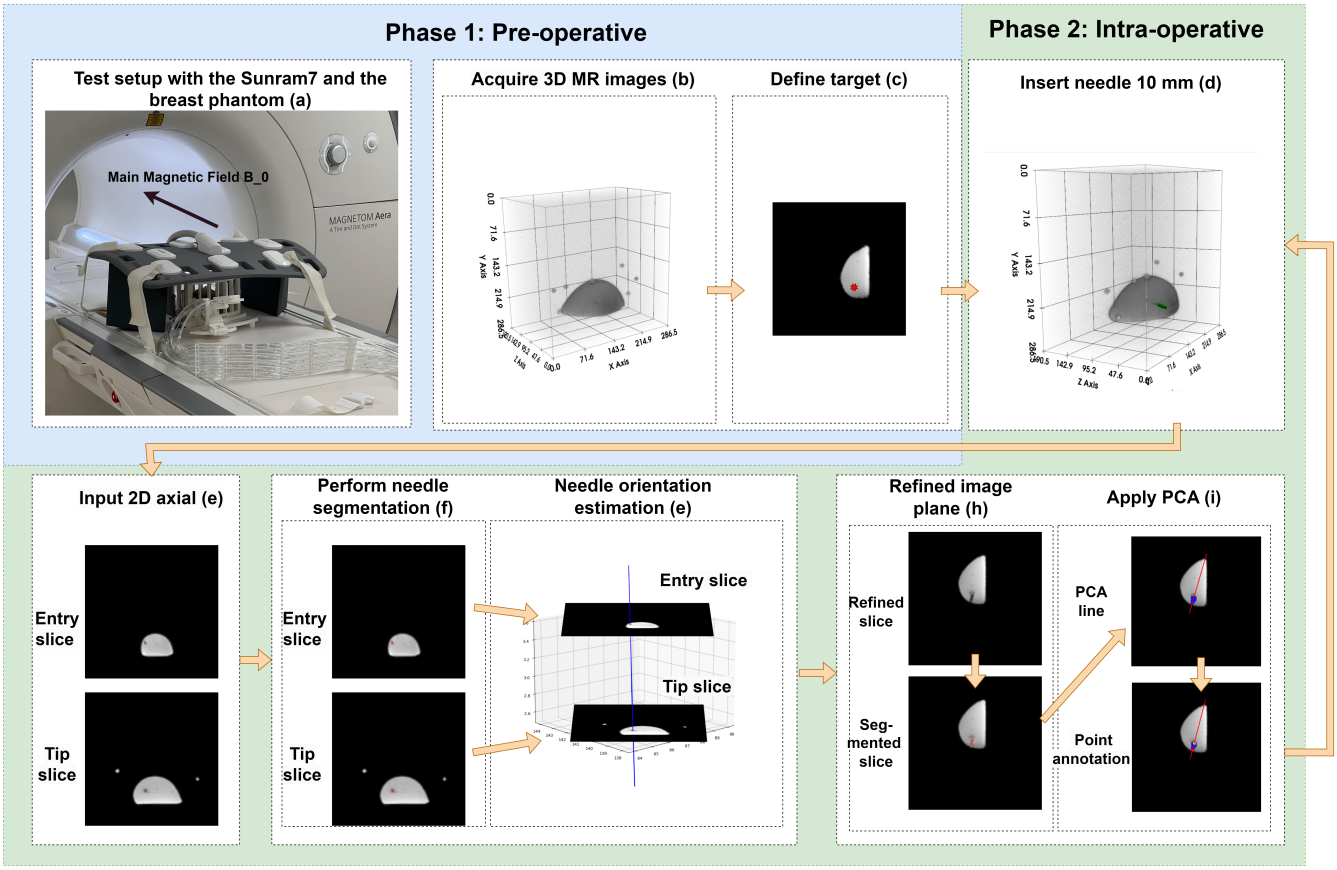

Fig. 4: The needle tracker algorithm consists of two primary phases: pre-operative and intra-operative. **(a)** The MRI scanner uses two separate coils for signal reception: an 18-channel torso coil and a 24-channel spine coil. **(b)** Acquiring 3D MR image to localize the lesion within the breast. As the 3D scan is also made to zero initialize the robotic system. **(c)** Initialize the position and orientation of the needle entry and the needle trajectory, corresponding to the lesion target. **(d)** Starts the Intra-operative section by inserting the needle 10 mm into the breast phantom. We use the calculated forward kinematics to obtain the initial position and orientation of the needle. This position and orientation are used to set the first MRI slice, with goal the reduce the processing time. **(e)** Aquire 2D Real-time MRI slices located at the entry and the tip position of the needle, orientated in the axial direction. **(f)** Perform needle segmentation using the YOLOv8-segmentation model, to obtain the position where the needle is located. **(g)** Perform orientation calculating, using the mean centre point of the segmented masks of the two axial slices. **(h)** Obtain the refined image plane, with use of the calculated needle orientation, and segment this using the YOLOv8-segmentation model. **(i)** Apply Principle Component Analysis on the point mask of the segmented mask of the refined image plane. By using the PCA first component and the point mask, we can annotate the intersection between these two elements corresponding to the entry and tip location. In the end, the Intra-operative phase will restart till the needle reaches the target lesion.

For training the model, an NVIDIA GeForce RTX3080 Laptop GPU was used along with Python v3.11.9, YOLOv8.0.196, Pytorch v2.2.0 and Cudav11.8. The training ran for up to 150 epochs with a batch size of 4, for 1.5 hours.

D. *Access-i*

Access-i, developed by Siemens Healthcare GmbH, is the platform that enables third-party clients to establish two-way communication with the MRI scanner of Siemens [17]. The communication is with the HTTPS GET and HTTPS POST requests. With the interface, third-party clients can remotely control various aspects of the MR scanner, including: Executing scans, and retrieving image data. This bi-directional communication and control capability opens up possibilities for integrating the MR scanner into the pipeline described in the previous part. By strategically adjusting the slice orientation and position of the slice groups, we can optimize image acquisition for needle tracking.

E. *System overview*

The workflow (Fig. 4) consists of two phases. In the pre-operative phase, the goal is to initialize the position of the Sunram7 and move the end-effector to the defined location. Whereas, the goal of Intra-operative is to obtain the optimal slice view of the needle and track the needle tip during insertion.

Phase 1: Pre-operative: The algorithm of this part is given at Algorithm 1. To start this phase (Fig. 4, b), a 3D T-2-weighted True Fast Imaging with Steady-State Precession sequence was acquired to obtain a 3D scan of the breast phantom. The specific target (Fig. 4, c) was then manually defined within this scan, where based on this specific target the inverse kinematics were calculated to define the required joint angles of the Sunram7. The Sunram7 controller received the intended joint angle and was moved to this position. The calculated position and orientation $(x, y, z, \theta_x, \theta_y, \theta_z)$ of the end-effector are used in Part 2. While a comprehensive examination of the control and path planning of the Sunram7 is beyond the scope of this paper, the findings from [18] serve as a foundation for our subsequent analysis.

Algorithm 1 Step 1: planning

1: Setup Sunram7 next to the breast phantom
2: Acquire 3D MR images
3: Initialization calibration
4: Operator defines the target
5: Calculate the inverse kinematics
6: Send Sunram7 controller the desired joint angles

Phase 2: Intra-operative Phase: During the Intra-operative phase, the patient table will not be moved out, as the robotic system will be used to move and insert the needle into the breast phantom. In the following part a more detailed explanation of algorithm 2 will be given.

Initialisation insertion: After phase 1, the needle is placed and orientated into the intended position. However, the needle is not visible on the MRI slices when the needle is outside the breast phantom. So to view the needle, an initialisation insertion of 10mm is done into the breast phantom (Fig. 4, d). After needle insertion, the calculated orientation and position are utilized to establish the initial refined MRI slice, enabling comprehensive visualization of the needle within a single plane

Coordinate systems: Conversion between the different coordinate systems ensures that points identified in the MRI image correspond precisely to their physical locations. This allows the robot to accurately target areas of interest within the patient. The field-of-view of the MRI scan is 288x288x192 mm, where each image plane has a dimension of 192x192 pixels, with an isotropic voxel size of 1.5 mm^2. Three coordinate systems are involved:

1) *DICOM Volume Coordinate System (DCS)*: DICOM volumes are typically stored with the origin at the top-left corner of the first slice. This means that the coordinates of the first voxel in the volume are (0, 0, 0) (Fig. 5 [left]).
2) *Patient Coordinate System (PCS)*: This is the real-world system where the robot operates. Its origin is at the isocenter, which is pinpointed using a laser at the beginning of the measurement. The units of this coordinate system are in mm (Fig. 5 [right]).
3) *Image Coordinate System (ICS)*: This is the coordinate system in which the MRI slice images are located. Its origin is at the top-left corner of the image, and it measures in pixel (Fig. 6).

1) DCS to PCS: Given a point in in the DCS in voxels ($P_{ICS} = [x, y, z]$), we can calculate this point in the PCS (Fig. 5). First we need to convert the point into mm, this is done by multiplying the point by the isotropic voxel size: $P_{mm} = P * 1.5mm/pixel$, so we get the vector: $P_{mm} = [x_{mm}, y_{mm}, z_{mm}, 1].T$. Next, we transform the point from the image coordinate system to the patient coordinate system: $P_{PCS} = T_{matrix} \cdot P_{mm}$, where T_{matrix} is the transformation matrix. The transformation matrix is shown in matrix 1. As seen here, there is a 4x4 matrix consists both a rotation and translation matrix. The rotation matrix consists of a column vector ($\vec{col}$), row vector ($\vec{row}$) and normal vector ($\vec{norm}$). $\vec{col}$ and $\vec{row}$ describe the direction of the image rows and image columns with respect to the patient's anatomical axes (Right-Left, Anterior-Posterior, and Foot-Head directions). The two vectors are obtained by the DICOM file tag (0x0020, 0x0037). As $\vec{norm}$ represents the direction perpendicular (normal) to the plane. This vector is orthogonal on the $\vec{row}$ and $\vec{column}$, so to obtain $\vec{norm}$ we calculate: $\vec{col} \cdot \vec{row}$. For the the translation matrix, we use the DICOM header (0020,1041) this is defined as the relative position of the image plane in with respect to the origin which is expressed in mm. Fig. 5, illustrates this conversion between the two coordinate systems, where the red cross corresponds the origin of both coordinate system. By applying the transformation matrix T on the point P_{mm}, we got the point in the PCS: $P_{PCS} = T_{matrix} \cdot P_{mm}$

$$T = \begin{bmatrix} norm_x & norm_y & norm_z & t_x \\ col_x & col_y & col_z & t_y \\ row_x & row_y & row_z & t_z \\ 0 & 0 & 0 & 1 \end{bmatrix} \quad (1)$$

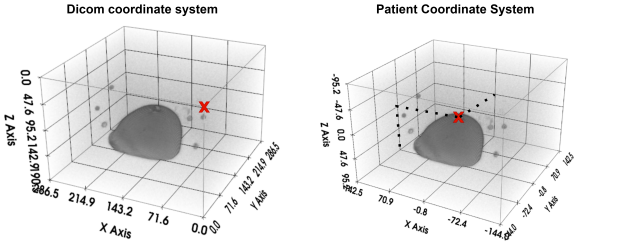

Fig. 5: Two coordinate systems showed on the left the DICOM Volume Coordinate System (DCS) and on the right the Patient Coordinate System (PCS). The origin of both coordinate system is marked with a red cross. As seen here the origin of the DCS is located at the corner of the volume compared with the PCS where the origin is located in the centre of the volume.

2) ICS to PCS: When obtaining the 2D oblique coronal slice, the tip point is defined by its x and y coordinates ($P_{image} = [x_1, y_1]$ in the 2D plane (Fig. 6). As the origin of the ICS is at the left upper voxel of the image, we need to translate P_{image} first to the centre of the image. By knowing the dimension of the image, we can find the centre of the image in PCS: $P_{mm} = P_{images} * 1.5mm/pixel - [\frac{height}{2}, \frac{width}{2}]$ in mm. Which results in the vector: $P_{mm} = [x_{mm}, y_{mm}, 0, 1.\text{T}$. As the origin of the slice is set with the slice position, we can obtain the 3D position of the origin of the 2D plane: $P_{origin_{pcs}} = [x_2, y_2, z_3]$ in mm. The vectors orthogonal on the plane is also known: $\vec{readout}$ and $\vec{phase}$. The following transformation matrix can be set up:

$$T = \begin{bmatrix} norm_x & norm_y & norm_z & x_2 \\ read_x & read_y & read_z & y_2 \\ phase_x & phase_y & phase_z & z_2 \\ 0 & 0 & 0 & 1 \end{bmatrix} \quad (2)$$

By applying the transformation matrix T on the point of the 2D slice P_{mm}, we can calculate the 3D coordinate of this point: $P_{3D} = T \cdot P_{mm}$ in the patient coordinate system.

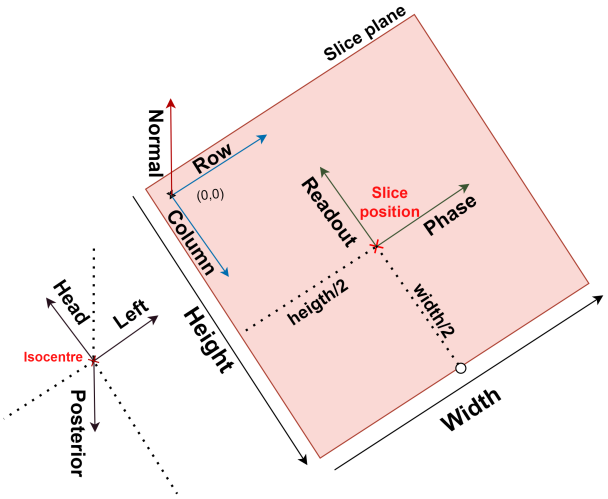

Fig. 6: In the Image Coordinate System (ICS), the origin is located at the left upper pixel. Whereas, the orientation of the slice is defined by the normal, phase and readout vectors. The slice position is used to set the centre of the slice plane to a position in an offset to the isocentre. The isocentre is in the RAS coordinate system. This means that the X-axis pointed to the patient's right, the Y-axis pointed anteriorly, and the Z-axis pointed superiorly.

Slice group orientation: Once the 3D position and orientation of the needle within the breast phantom are known, three sets of slices can be created. Two of these sets are oriented in the axial direction: one at the point where the needle enters the phantom and the other at the needle's tip (Fig. 7, middle and right). These two sets of slices allow for the estimation of the needle's main axis orientation using the centre point of the segmented needle masks. Assign coordinates (x1, y1, z1) and (x2, y2, z2) to the two points. And subtract the coordinates of the first point from the coordinates of the second point to obtain (dx = (x2-x1), dy = (y2-y1), dz = (z2-z1). Divide each component of the direction vector by its magnitude ($\sqrt{(dx^2 + dy^2 + dz^2)}$) then we got the main axis orientation (normalized_dx = $\frac{dx}{magnitude}$, normalized_dy = $\frac{dy}{magnitude}$, normalized_dz = $\frac{dz}{magnitude}$). The final slice is set in the refined oblique orientation which provides a complete view of the needle (Fig. 7, left).

The MRI uses the RAS coordinate system. To set the slice orientation of the MRI, three vectors need to be determined: normal ($\vec{n}$), phase ($\vec{p}$) and read vector ($\vec{r}$). The three vectors form an orthogonal coordinate system. This system defines the plane in which the MRI image slice will lie, and also the direction in which the image data will be acquired. The $\vec{n}$ is perpendicular to the plane of the slice. This $\vec{n}$ is calculated by the PCA. Whereas the $\vec{p}$, lies within the plane of the slice and dictates the direction along which phase encoding gradients are applied. To find the $\vec{p}$, we used the Gram-Schmidt method. First, an arbitrary vector with a unity length is chosen where it is not parallel to the $\vec{n}$: $\vec{w1}$ = $[1, 0, 0]$ or $[0, 1, 0]$. This vector is not necessarily orthogonal to the normal vector at this point. It's only an arbitrary vector that will be used to calculate the phase vector later. In the next step, we calculated the projection w1 onto the n vector: $proj\_w1 = (\vec{w1} \cdot \vec{n}) * \vec{n}$. By subtracting the project from $proj\_w1$, we got the orthogonal vector: $\vec{p} = \vec{n} - proj\_w1$

At last, the readout vector $\vec{r}$ is also within the slice plane and is orthogonal to $\vec{n}$ and $\vec{p}$. It's the direction along which frequency encoding gradients are applied. This vector is calculated by taking the cross product of the $\vec{n}$ and $\vec{p}$: $\vec{r} = \vec{n} \times \vec{p}$. Furthermore, there are key requirements for the input vectors.

1) Normalized: each vector must have a magnitude of 1.
2) Conventionalized: the largest component (x, y, or z) of each vector must be positive.
3) Orthogonal: All three vectors must be mutually perpendicular (orthogonal) to each other.
4) Right-Hand Rule: The vectors must adhere to the right-hand rule: normal = phase x read

Needle segmentation: YOLOv8-segmentation was applied to the MRI images. By defining the needle as the only non-background class, the model can focus on identifying the needle from the rest of the image content. The output of the model will be the bounding boxes of the location of the needle and within the bounding boxes a segmentation of the needle feature. As seen in the output of Fig. 3.

Filter out the false positive: To filter out incorrect detections (false positives), we use a "region of interest" (ROI). We can know from step 1 where the Sunram7 end-effector should be using its position and orientation $(x, y, z, \theta_x, \theta_y, \theta_z)$. This helps us define the ROI. If the needle segmentation masks are predicted outside this area, we know they're false positive predictions.

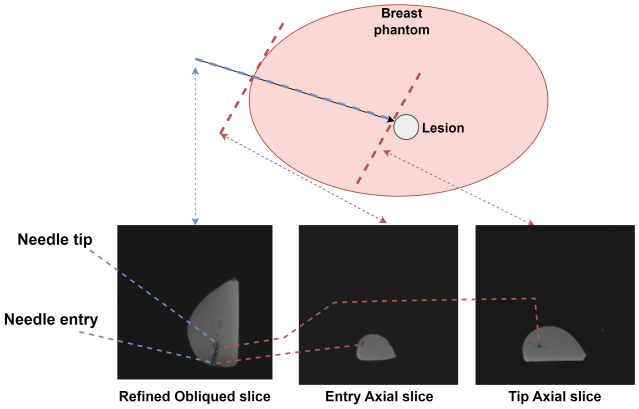

Fig. 7: The schematic overview shows the three slices method. The refined obliqued slice on the left side is the MRI slice where the biospy needle is fully seen. This slice is used to keep track of any movement in the needle entry and tip point. The middle and right side are the MRI slices where the needle entry and tip are seen in the axial orientation. These two slices have the function of keeping track of the orientation of the needle trajectory. With this correction in the slice orientation, the refined slice always shows the needle fully in one slice.

Principle Components Analysis (PCA)*:* PCA is a technique that reduces the dimensionality of a dataset while preserving the most important information.

1) Calculate the mean: Find the average value for each dimension of the point cloud.
2) Compute the covariance matrix: This matrix measures how much the variables in the dataset vary together.
3) Determine principal components: The principal components are the eigenvectors of the covariance matrix, representing the directions of maximum variance.
4) Sort principal components: Sort the principal components in descending order based on their corresponding eigenvalues. The first principal component (PC1) represents the direction of maximum variance.

In the case of needle entry and tip position estimation, PC1 can be used as an estimate of the needle's main axis.

Oblique slice*:* Extracting a 2D oblique plane from a 3D volume involves specifying a point of interest and a normal vector. The normal vector, perpendicular to the image plane, dictates the direction the MRI slice faces. The slice position defines the location the slice plane must pass through. The calculated orientation of the two-point of the entry and tip point serves as the normal vector (refer to Fig.8 for a visual representation). The needle tip location of the axial segmentation mask is initially selected as the point of interest. To refine the oblique slice and ensure optimal full needle visualization, an iterative search is employed. This process involves exploring neighbouring positions and evaluating needle detection confidence to identify the most suitable slice plane.

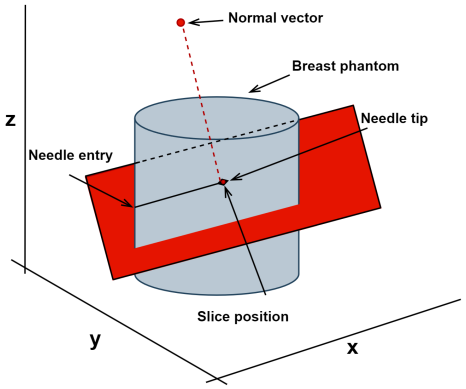

Fig. 8: A simplified schematic of the breast phantom in the form of a cylinder. The slice orientation is according to the normal vector. The slice position is on the needle tip.

Annotate needle tip and entry point*:* Once the oblique slice is acquired, the needle tip and entry point need to be pinpointed. The oblique slice is again segmented using YOLOv8. Principal Component Analysis (PCA) is leveraged to identify the needle's long axis. The points where this PCA line first and last intersect the needle mask are designated as the entry point and tip, respectively. To track needle movement, movement analysis is performed on the needle tip. Based on the previous tip estimation, the direction of movement (backwards or forward) can be determined. This information is used to adjust the axial begin and end slice based on the different movements observed.

Algorithm 2 part 2: Real-time tracking

1: Send command to Sunram7 to insert the needle 10 mm
2: Setup two oblique axial slice groups
3: Perform YOLOv8 image segmentation on the two axial slices
4: Filter out false positive predictions
5: Use segmentation points to estimate the needle orientation
6: Setup one refined 2D slice group and search the point of interest
7: Perform YOLOv8 image segmentation on the refined 2D MRI slice
8: Apply PCA to annotate the needle tip and entry point
9: Check needle movement
10: Go back to step 1

IV. Evaluation Metrics

In evaluating the performance of the YOLOv8 segmentation model on the given dataset, mAP (mean Average Precision) provides a quantification of how well the model performs in terms of precision and recall. A higher mAP indicates better performance. Additionally, we consider mAP@50 and mAP@50-90.

Subsequently, the accuracy of the 3D needle tip localization will be assessed. We evaluate the 3D needle tip of 11 trials, where the insertion depth varies between 18.43 mm

to 60.98 mm. After each trial, a 3D MRI scan was acquired as ground truth. The Euclidean distance between the human-verified and estimated tip points was calculated to determine the accuracy of 3D needle tip localization

Next, a biopsy needle will be inserted into the breast phantom using the robotic system. During the experiments, a lesion target is set. This target is inside of the breast phantom, which is a cube-shaped target of a size of 23x14x7 mm^3, this cube should mimic the lesion inside of the breast. In the first experiment, the robotic system solely relied on the planned trajectory to reach the target. In the second experiment, real-time needle tracking was used to monitor the needle's position. If the needle deviates from the target, the robotic system will carefully retract the biopsy needle 10 mm and re-orientate it under image guidance to relocate the biopsy needle to the right trajectory. This process of needle adjustment will be repeated as necessary until the needle tip is accurately placed within the target positions. The success rate of hitting the intended target is measured. And the success rate of frames in which the needle is accurately detected within the MRI scans.

In the final experiment, the real-time needle tracking system's processing speed was evaluated. This involved measuring the MRI acquisition time and the processing time of the needle-tracking pipeline.

V. Results

A. Segmentation

Figure 9 shows the results of the model's predictions on the test dataset. This demonstrates the model's strong performance in predicting the needle component. After training the model reached a mAP@50 of 0.822 for the axial and 0.968 for the refined oblique slice. This indicates that the model is highly effective at detecting and localizing objects. However, the mAP dropped to 0.346 and 0.558 respectively when considering a wider range of IoU thresholds from 50% to 95% (mAP@50-95) (table II).

TABLE II: Evaluation metrics of the YOLOv8 segmentation model

Class	Precision	Recall	mAP50	mAP50-95
Axial	0.835	0.828	0.822	0.346
Refined	0.957	0.982	0.968	0.558

B. 3D needle tip localization

To evaluate the accuracy of the needle tracker algorithm, the estimated tip positions were compared to human-verified positions determined through manual analysis of 3D MRI scans, Figure 10 shows both from the real-time algorithm and the human-verified tip annotation. Over 11 trials, the Euclidean distance between the estimated and human-verified tip positions was calculated (Table III). The average 3D tip localization accuracy was found to be 1.179 $\pm$ 0.385 mm.

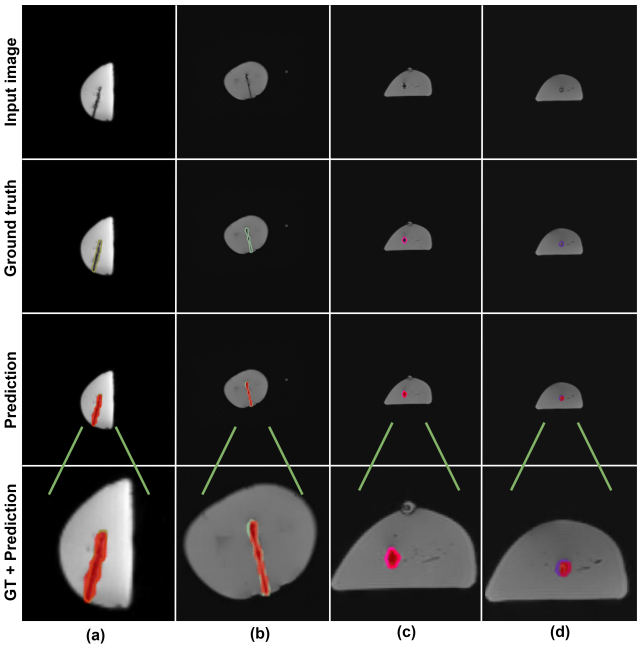

Fig. 9: Example of 2D needle feature segmentations. The input image is shown in the first row. Here (a) and (b) represent the refined oblique slice and (c) and (d) the axial-orientated slice. The ground truth label is shown in the second row, as in the third row the predict masks. The last row is used to zoom in scale to compare the predicted and ground truth labels. As can be seen the red at (a)/(b) and pink (c)/(d) segments are the predicted masks.

TABLE III: Trial accuracy of 3D needle tip localization

Trial	Offset [mm]	Trial	Offset [mm]
1	0.8432	7	0.9007
2	1.5581	8	1.4663
3	0.9257	9	1.3132
4	1.5683	10	0.7326
5	0.8929	11	1.9385
6	0.8295		
Average		1.179 $\pm$ 0.385	

C. Biopsy based on visual guidance

Figure 11 illustrates the results of two biopsy attempts targeting the same lesion. In the first attempt, relying solely on the forward kinematics of the Sunram7, the biopsy needle missed the target, resulting in no lesion tissue acquisition. In contrast, in the second experiment, we did an attempt where the robotic system corrected the biopsy needle trajectory based on the visual feedback of the real-time needle tracking. By continuously monitoring the needle's position and orientation, the robotic system reached the target lesion and obtained tissue samples successfully, Figure 12 shows the trajectory of this biopsy attempt. During the second experiment, 963 MRI slice frames were acquired, providing the necessary data for the real-time tracking algorithm to determine the needle's trajectory and tip position accurately.

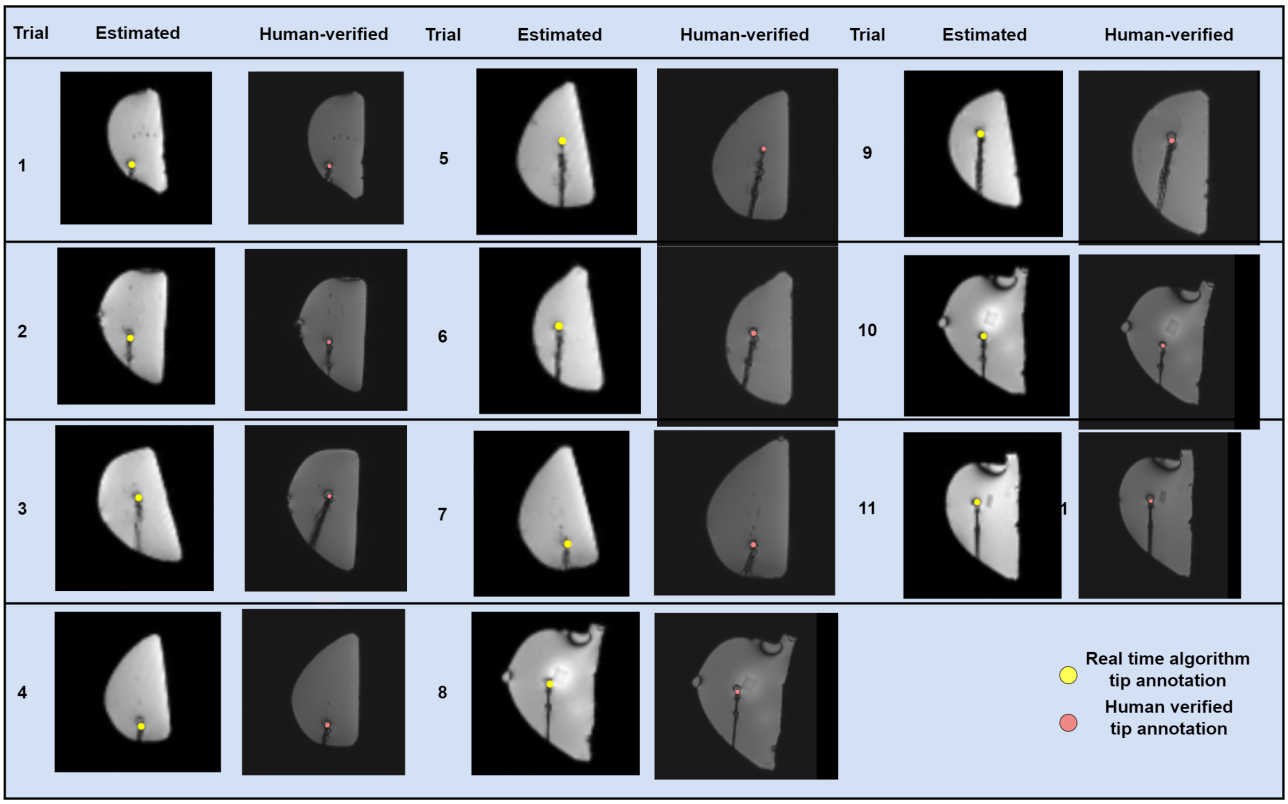

Fig. 10: 11-trial experiments assessed the 3D needle tip localization accuracy of the real-time algorithm. Tip positions were estimated (yellow dot) and compared against manual annotations from the 3D scan (red dot) across insertion distances ranging from 18.43 mm to 60.98 mm.

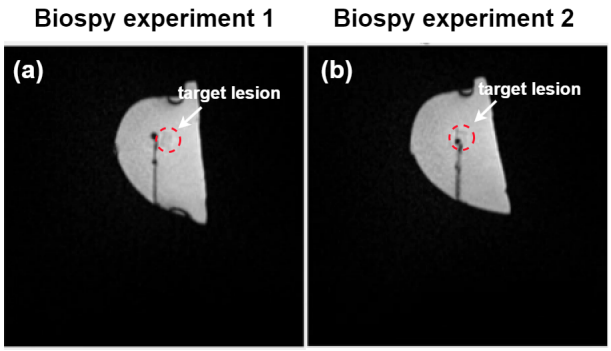

Fig. 11: Comparison of biopsy outcomes using the Sunram7 robotic system. (a) A missed biopsy occurred when relying solely on forward kinematics. (b) The addition of real-time visual feedback enabled successful targeting of the same lesion, demonstrating the effectiveness of visual guidance for accurate needle placement.

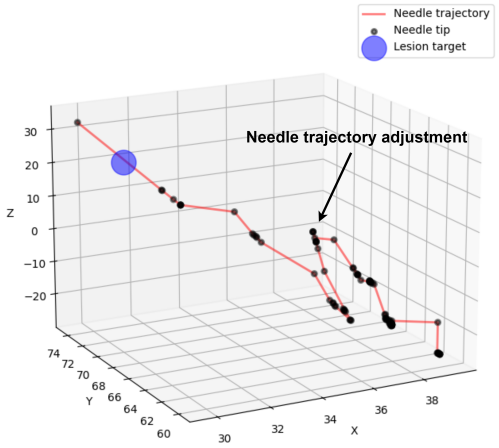

Fig. 12: The red line represents the needle tip trajectory in experiment 2, with black dots marking the needle tip positions. Needle retraction was utilized to align the trajectory with the lesion target.

D. Processing time

The Access-i interface acquired images at a rate of 288.96 ms per slice, while the average segmentation time was approximately 40 ms per MRI slice. Remote control commands to the MR scanner were transmitted and acknowledged within 13 ms. Next, the analysis of the real-time processing pipeline was divided into two parts. The first stage, consisting of needle orientation estimation from two 2D axial slices and the identification of the optimal refined slice (Fig. 4 parts (h) to (i)), took an average time of 10.35 seconds. The second stage, involving the annotation of the needle tip and entry position on the refined image plane (Figure 4 (h)), had

an average processing time of 1.63 seconds. When needle orientation estimation was necessary, the total pipeline time averaged 11.98 seconds. However, in the absence of detected movement, the refined slice did not require adjustment, reducing the total time to 1.63 seconds. Figure 13 illustrates the output interface, displaying the segmented axial slice in the left and middle images and the segmented refined oblique slice with annotated needle tip (yellow), entry point (red), and needle trajectory (red line) in the right image. The entire biopsy procedure, including 3D scanning, target lesion identification, and tissue acquisition, was completed in approximately 13.5 $\pm$ 2.5 minutes.

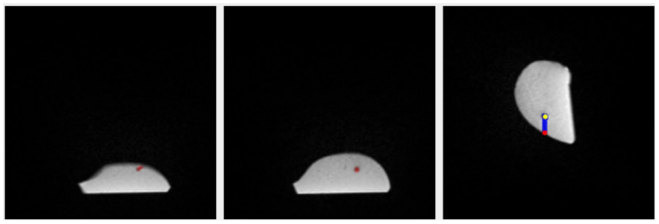

Fig. 13: The output screen is shown to see the result of the prediction. Using real-time input coming from the MRI. **(a)** We have put the axial-orientated slice at the entry slice. (b) We have put the axial-orientated slice at the tip slice. The predicted masks are shown with a red annotation. (c) We find the refined oblique slice. Where the entry point is annotated with a red dot and the tip point is annotated with a yellow point. The red line is the main axis of the needle, showing the trajectory of the needle.

VI. Discussion

This study introduces a real-time tracking algorithm capable of monitoring a biopsy needle within an MRI environment using 3 intra-procedural 2D MRI scans. For training the segmentation mode 53 3D and 701 2D images were used. Segmentation results showed effectively detected needle appearances in the MRI scans. Notably, this dataset is significantly smaller than that employed in [12], which utilized 583 T2-weighted intra-procedural MRI scans. The proposed pipeline required only three MRI slices for accurate needle orientation and position estimation. The results demonstrate the system's efficacy in facilitating real-time visual guidance for the robotic system. The achieved 3D needle tip localization accuracy of 1.179 ± 0.385 mm is comparable to other reported results (Table IV). During the biopsies, the needle could be tracked from all of the frames. By having such visual feedback the accuracy of the robotic system's biopsy trajectory would be not only dependent on the forward kinematics. Such visual feedback obtained from the proposed method would thus be used for the feedback control loop to enable dynamic trajectory adjustment for MRI safe biopsy robot. Furthermore, the biopsies took 13.5 $\pm$2.5 min, which indicated less required time than traditional which has an average time of 38 min per biopsy [19].

Although the proposed system is functional, certain limitations exist. The insertion speed is presently constrained by the pipeline's processing speed. The real-time needle tracking algorithm required starting from its initial position, an average of 11.98 seconds to estimate the needle position. While this processing time is not functionally problematic for the current needle insertion rate of 10 mm per iteration, it may hinder achieving arbitrarily high insertion speeds. To address this, parallelizing various stages of the pipeline could potentially reduce the overall processing time. Additionally, the study did not involve in-vivo experiments, which is why the training dataset lacks in vivo data. Consequently, the segmentation model is not yet prepared for clinical trials. To facilitate future clinical trials, it is important to conduct more extensive research, with a particular focus on in vivo experiments. As obtaining vivo dataset is in general very difficult, the use of simulated data could be explored to generalize and extend this segmentation dataset.

TABLE IV: Accuracy's compared with other works

	Proposed	[9]	[10]	[11]
Accuracy [mm]	1.179 $\pm$ 0.385	0.9	0.96 $\pm$ 0.69	1.48

VII. Conclusion

In this study, we propose a novel method for tracking biopsy needles in an MRI environment using the three-slice approach. By strategically positioning axial slices at the needle entry and tip, we accurately estimate the needle's orientation, enabling the acquisition of a refined oblique slice that consistently captures the entire needle. Our method demonstrated comparable accuracy to existing approaches (Table IV), with an average error of 1.179 ± 0.385 mm. With this approach, it's possible to provide the robotic system with real-time visual feedback of the needle's position. Enabling the function to dynamically adjust the needle trajectory during insertion. This real-time visual feedback system can be applied to any MRI application that requires visual guidance of needle position.

VIII. Acknowledgment

We would like to thank Marjon Kuipers for her contributions to helping and producing the breast phantoms. Additionally, we extend our thanks to Jaap Greve and Remco Liefers for their expert guidance and assistance in MRI-related matters.

References

[1] [Online]. Available: https://www.who.int/news/item/03-02-2023-who-launches-new-roadmap-on-breast-cancer

[2] Y.-S. Sun, Z. Zhao, Z.-N. Yang, F. Xu, H.-J. Lu, Z.-Y. Zhu, W. Shi, J. Jiang, P.-P. Yao, and H.-P. Zhu, "Risk factors and preventions of breast cancer," *International Journal of Biological Sciences*, vol. 13, no. 11, p. 1387–1397, 2017.

[3] R. T. Blanco, R. Ojala, J. Kariniemi, J. Perälä, J. Niinimäki, and O. Tervonen, "Interventional and intraoperative mri at low field scanner – a review," *European Journal of Radiology*, vol. 56, no. 2, pp. 130–142, 2005, new Frontiers in Diagnostic Imaging. [Online]. Available: https://www.sciencedirect.com/science/article/pii/S0720048X05001221

[4] H. Ranjan, M. Van Hilten, V. Groenhuis, J. Verde, A. Garcia, S. Perretta, J. Veltman, F. J. Siepel, and S. Stramigioli, "Sunram 7: An mr safe robotic system for breast biopsy," *2023 IEEE/RSJ International Conference on Intelligent Robots and Systems (IROS)*, Oct 2023.

[5] H. Liu, W. A. Hall, A. J. Martin, and C. L. Truwit, "Biopsy needle tip artifact in mr-guided neurosurgery," *Journal of Magnetic Resonance Imaging*, vol. 13, no. 1, p. 16–22, Jan 2001.

[6] L. Cai, J. Gao, and D. Zhao, "A review of the application of deep learning in medical image classification and segmentation," *Annals of Translational Medicine*, vol. 8, no. 11, p. 713–713, Jun 2020.

[7] M. H. Hesamian, W. Jia, X. He, and P. Kennedy, "Deep learning techniques for medical image segmentation: achievements and challenges," *Journal of digital imaging*, vol. 32, pp. 582–596, 2019.

[8] B. Kayalibay, G. Jensen, and P. van der Smagt, "Cnn-based segmentation of medical imaging data," *arXiv preprint arXiv:1701.03056*, 2017.

[9] X. Li, A. S. Young, S. S. Raman, D. S. Lu, Y.-H. Lee, T.-C. Tsao, and H. H. Wu, "Automatic needle tracking using mask r-cnn for mri-guided percutaneous interventions," *International Journal of Computer Assisted Radiology and Surgery*, vol. 15, no. 10, p. 1673–1684, Jul 2020.

[10] X. Li, Y.-H. Lee, D. S. Lu, T.-C. Tsao, and H. H. Wu, "Physics-driven mask r-cnn for physical needle localization in mri-guided percutaneous interventions," *IEEE Access*, vol. 9, pp. 161 055–161 068, 2021.

[11] W. Zhou, X. Li, F. Zabihollahy, D. S. Lu, and H. H. Wu, "Deep learning-based automatic pipeline for 3d needle localization on intra-procedural 3d mri," *International Journal of Computer Assisted Radiology and Surgery*, Mar 2024.

[12] A. Mehrtash, M. Ghafoorian, G. Pernelle, A. Ziaei, F. G. Heslinga, K. Tuncali, A. Fedorov, R. Kikinis, C. M. Tempany, W. M. Wells, and et al., "Automatic needle segmentation and localization in mri with 3-d convolutional neural networks: Application to mri-targeted prostate biopsy," *IEEE Transactions on Medical Imaging*, vol. 38, no. 4, p. 1026–1036, Apr 2019.

[13] B. Dwyer, J. Nelson, T. Hansen *et al.*, "Roboflow," https://roboflow.com, 2024, [Software].

[14] G. Jocher, A. Chaurasia, and J. Qiu, "Ultralytics YOLO," Jan. 2023. [Online]. Available: https://github.com/ultralytics/ultralytics

[15] K. He, G. Gkioxari, P. Dollar, and R. Girshick, "Mask r-cnn," in *Proceedings of the IEEE International Conference on Computer Vision (ICCV)*, Oct 2017.

[16] O. Ronneberger, P. Fischer, and T. Brox, "U-net: Convolutional networks for biomedical image segmentation," in *Medical Image Computing and Computer-Assisted Intervention – MICCAI 2015*, N. Navab, J. Hornegger, W. M. Wells, and A. F. Frangi, Eds. Cham: Springer International Publishing, 2015, pp. 234–241.

[17] R. Schneider and D. Franger, "Mr access-i developer guide version 1.1.2 for nx (11337213-asd-aci-01)," 2021, [Software].

[18] I. Kuijper, "An interactive approach for mri-based interventional navigation," Oct 2024.

[19] C. D. Lehman, E. R. DePeri, S. Peacock, M. D. McDonough, W. B. DeMartini, and J. Shook, "Clinical experience with mri-guided vacuum-assisted breast biopsy," *American Journal of Roentgenology*, vol. 184, no. 6, pp. 1782–1787, 2005.